Front. Environ. Sci. Eng. 2022, 16(5): 60
https://doi.org/10.1007/s11783-022-1539-2

RESEARCH ARTICLE

CeO_2 doping boosted low-temperature NH_3-SCR activity of $FeTiO_x$ catalyst: A microstructure analysis and reaction mechanistic study

Wei Tan[1,2], Shaohua Xie[1], Wenpo Shan[3,4], Zhihua Lian[3,4], Lijuan Xie[3], Annai Liu[5], Fei Gao[2], Lin Dong[2], Hong He[3,4], Fudong Liu (✉)[1]

1 Department of Civil, Environmental, and Construction Engineering, Catalysis Cluster for Renewable Energy and Chemical Transformations (REACT), NanoScience Technology Center (NSTC), University of Central Florida, Orlando, FL32816, USA
2 Key Laboratory of Mesoscopic Chemistry of MOE, School of Chemistry and Chemical Engineering, Jiangsu Key Laboratory of Vehicle Emissions Control, School of Environment, Center of Modern Analysis, Nanjing University, Nanjing 210023, China
3 State Key Joint Laboratory of Environment Simulation and Pollution Control, Research Center for Eco-Environmental Sciences, Chinese Academy of Sciences, Beijing 100085, China
4 Key Laboratory of Urban Pollutant Conversion, Institute of Urban Environment, Chinese Academy of Sciences, Xiamen 361021, China
5 Institute of Engineering Technology, Sinopec Catalyst Co. Ltd., Sinopec Group, Beijing 101111, China

HIGHLIGHTS

- CeO_2 doping significantly improved low-temperature NH_3-SCR activity on $FeTiO_x$.
- The crystallinity of $FeTiO_x$ was decreased dramatically after CeO_2 doping.
- Unique Ce-O-Fe structure in $FeCe_{0.2}TiO_x$ accounted for its superior redox property.
- Facile activation of NH_3 to -NH_2 on $FeCe_{0.2}TiO_x$ promoted the $DeNO_x$ efficiency.

GRAPHIC ABSTRACT

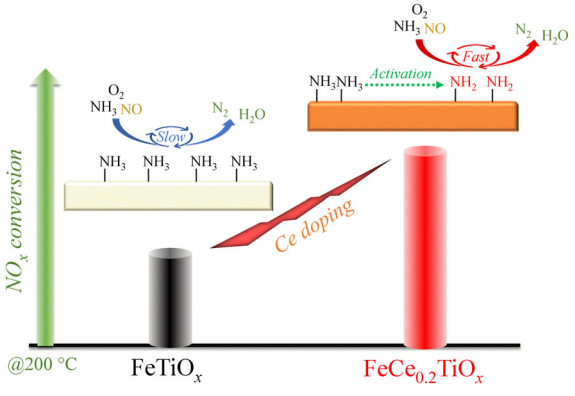

ARTICLE INFO

Article history:
Received 3 November 2021
Revised 19 December 2021
Accepted 21 December 2021
Available online 26 January 2022

Keywords:
NH_3-SCR
CeO_2 doping
Low-temperature NO_x removal
Improved redox property
In situ XAFS analysis

ABSTRACT

$FeTiO_x$ has been recognized as an environmental-friendly and cost-effective catalyst for selective catalytic reduction (SCR) of NO_x with NH_3. Aimed at further improving the low-temperature $DeNO_x$ efficiency of $FeTiO_x$ catalyst, a simple strategy of CeO_2 doping was proposed. The low-temperature (< 250 °C) NH_3-SCR activity of $FeTiO_x$ catalyst could be dramatically enhanced by CeO_2 doping, and the optimal composition of the catalyst was confirmed as $FeCe_{0.2}TiO_x$, which performed a NO_x conversion of 90% at *ca.* 200°C. According to X-ray diffraction (XRD), Raman spectra and X-ray absorption fine structure spectroscopy (XAFS) analysis, $FeCe_{0.2}TiO_x$ showed low crystallinity, with Fe and Ce species well mixed with each other. Based on the fitting results of extended X-ray absorption fine structure (EXAFS), a unique Ce-O-Fe structure was formed in $FeCe_{0.2}TiO_x$ catalyst. The well improved specific surface area and the newly formed Ce-O-Fe structure dramatically contributed to the improvement of the redox property of $FeCe_{0.2}TiO_x$ catalyst, which was well confirmed by H_2-temperature-programmed reduction (H_2-TPR) and *in situ* XAFS experiments. Such enhanced redox capability could benefit the activation of NO and NH_3 at low temperatures for NO_x removal. The detailed reaction mechanism study further suggested that the facile oxidative dehydrogenation of NH_3 to highly reactive -NH_2 played a key role in enhancing the low-temperature NH_3-SCR performance of $FeCe_{0.2}TiO_x$ catalyst.

✉ Corresponding author
E-mail: fudong.liu@ucf.edu

Special Issue—Frontier Progresses from Chinese-American Professors of Environmental Engineering and Science (Responsible Editors: Xing Xie, Jinkai Xue, Hongliang Zhang)

1 Introduction

Nitrogen oxides (NO_x) have been recognized as major air pollutants, which can lead to various environmental problems (He et al., 2002; Gan et al., 2021). It has been widely reported that selective catalytic reduction (SCR) of NO_x with NH_3 was one of the most effective technologies for NO_x elimination (Han et al., 2019; Chen et al., 2021). The toxicity and the poor low-temperature $DeNO_x$ efficiency for the commercial V_2O_5-WO_3 (MoO_3)/TiO_2 catalysts, and the high cost of zeolite catalysts have made it urgent to develop an efficient and non-toxic metal oxide SCR catalyst. In our previous studies, an environmental-friendly iron titanate ($FeTiO_x$) catalyst exhibiting excellent NH_3-SCR activity as well as satisfactory resistance to SO_2/H_2O poisoning in the medium-temperature range was developed (Liu et al., 2008; Liu et al., 2010). However, the NO_x elimination performance of such iron titanate catalyst was not satisfactory for the NO_x removal in the low-temperature range (e.g., below 200 °C) especially under the increasingly tightening NO_x emission standards.

Recently, many efforts have been devoted to developing new NH_3-SCR catalysts for low-temperature NO_x removal (Inomata et al., 2021; Ji et al., 2021; Kwon et al., 2021; Tan et al., 2021c; Zhang et al., 2021b). Using CeO_2 as active species, promoter or even support for low-temperature NH_3-SCR catalysts was one of the most popular strategies, due to the excellent redox property, relatively abundant reserves and low price of CeO_2 (Tang et al., 2016). Lee et al. prepared a CeO_2 promoted Sb-V_2O_5/TiO_2 catalysts, which exhibited enhanced low-temperature NH_3-SCR performance and satisfactory resistance to H_2O and SO_2 (Lee et al., 2013). It was reported that the addition of CeO_2 had a promotion effect as well on Cu-zeolite catalysts for improving low-temperature NO_x elimination efficiency and hydrothermal stability (Wang et al., 2016; Wang et al., 2020a). Mixed oxide materials containing CeO_2 (e.g., CeO_2-MnO_2, CeO_2-SiO_2, CeO_2-TiO_2, etc.) could also be used as efficient NH_3-SCR catalysts (Qi and Yang, 2003; Li et al., 2017; Tan et al., 2021a; Zeng et al., 2021). In these works, the addition of CeO_2 promoted the redox capacity at low-temperature range notably and well modified the surface acidity, which were vital for the enhancement of the low-temperature $DeNO_x$ efficiency.

In our previous work, CeO_2 doping was proved to be a simple but effective strategy to enhance the low-temperature NO elimination efficiency of $FeTiO_x$ catalyst, and the increased NO_x removal efficiency at low temperature mainly resulted from the enhanced dispersion of FeO_x and TiO_x species due to Ce addition, which then facilitated the adsorption/activation of NO_x and NH_3 simultaneously (Zhang et al., 2020). In present work, we investigated the CeO_2 promoted $FeTiO_x$ catalysts for NH_3-SCR of NO_x within a broader Ce doping range, focusing on the elucidation of local microstructure and redox property as well as the SCR mechanism using a series of *ex situ* and *in situ* advanced characterization techniques. The newly formed Ce-O-Fe structure was clearly demonstrated by *ex situ* X-ray absorption fine structure spectroscopy (XAFS) and the significant improvement of redox property of CeO_2 doped $FeTiO_x$ catalyst was well confirmed by H_2-temperature-programmed reduction (H_2-TPR) and *in situ* XAFS experiments. Detailed reaction mechanism study showed that the more facile oxidative dehydrogenation of NH_3 to form highly reactive -NH_2 species on CeO_2 doped $FeTiO_x$ was crucial for the promotion of its low-temperature NO_x elimination efficiency.

2 Materials and methods

2.1 Catalyst preparation

Fe-Ce-TiO_x catalysts were prepared by a homogeneous co-precipitation method, and $Fe(NO_3)_3 \cdot 9H_2O$, $Ce(NO_3)_3 \cdot 6H_2O$ and $Ti(SO_4)_2$ were used as precursors. The Fe-Ti and Fe-Ce molar ratios were set at 1:1 and 1:*a* (*a* = 0.1, 0.2, 0.6, 1 and 1.6), respectively. The calculated amount of $Fe(NO_3)_3 \cdot 9H_2O$, $Ce(NO_3)_3 \cdot 6H_2O$ and $Ti(SO_4)_2$ was first dissolved into deionized water. Excessive urea dissolved in deionized water was used as a precipitator. After that, the mixture was heated to 90 °C and kept there for 12 h under stirring. Then, the mixture was filtered and the obtained precipitate cake was washed with distilled water several times, followed by the desiccation at 100 °C for 12 h. Finally, the solid was calcined in air at 500 °C for 3 h. The prepared samples were named as $FeCe_aTiO_x$. Before the catalytic performance evaluation, all samples were pressed into tablets and then sieved into 40–60 mesh. All chemicals used in this work were purchased from Sinopharm Chemical Reagent Co., Ltd., China, and were of analytical grade without further purification.

2.2 Characterizations

The specific surface areas of the prepared catalysts were measured on a Quantachrome Quadrasorb SI-MP instrument (USA), using N_2 adsorption-desorption isotherms at – 196 °C by the Brunauer-Emmett-Teller (BET) method. The partial pressure range used for the calculation was 0.05–0.35. Prior to the test, the catalysts were degassed in vacuum at 300 °C for 4 h.

Powder X-ray diffraction (XRD) patterns were obtained from a PANalytical X'Pert Pro Diffractometer instrument (Netherlands), equipped with a Cu Kα radiation (λ = 0.15406 nm) source. The 2θ ranged from 10° to 80°, and the scanning speed was 7°/min. The step size was determined as 0.07°.

Raman spectroscopy experiment was conducted on a Spex 1877 D triplemate spectrograph (USA), which used a DPSS diode-pump solid semiconductor laser (λ = 532 nm) as the excitation source, and the output power was set at

40 mW.

The *ex situ* XAFS of Fe K-edge and Ce K-edge in $FeTiO_x$ and $FeCe_aTiO_x$ catalysts (a = 0.1, 0.2, 0.6, 1 and 1.6) were collected in transmission mode on BL-7C and NW10A beamlines, respectively, Photon Factory, High Energy Accelerator Research Organization (KEK), Japan. Pure Fe_2O_3 and CeO_2 were used as reference samples. The *in situ* XAFS of Fe K-edge in $FeTiO_x$ and $FeCe_{0.2}TiO_x$ catalysts during the H_2-temperature-programmed reduction (H_2-TPR) process were recorded in transmission mode by a quick XAFS (QXAFS) method on BL-12C beamline, Photon Factory, KEK, Japan. During the H_2-TPR process, samples were exposed to a flow of 5 vol.% H_2/He, heated from room temperature to 900 °C. REX2000 program (Rigaku Co., Japan) was applied to analyze the XAFS data. XANES were normalized based on edge height. EXAFS oscillation $\chi(k)$ was extracted using spline smoothing with a Cook-Sayers criterion (Cook and Sayers, 1981), and the filtered k^3-weighted $\chi(k)$ was Fourier transformed into R space in the k range of 2.0–13.0 $Å^{-1}$ for Fe-K edge and 2.0–14.0 $Å^{-1}$ for Ce-K edge. During the curve fitting process, FEFF8.4 code was used to calculate the possible backscattering amplitude and phase shift (Ankudinov et al., 1998).

X-ray Photoelectron Spectroscopy (XPS) experiments were carried out on Scanning X-ray Microprobe (PHI Quantera, ULVAC-PHI, Inc., Japan), using a monochromatic Al K radiation source (1486.7 eV). C 1s line at 284.6 eV was used to calibrate the binding energies (BE) of all the elements.

H_2-TPR experiments were carried out on an AutoChem 2920 Chemisorption Analyzer (Micromeritics, USA). Before the measurement, catalysts were first pretreated in flowing air (50 mL/min) at 300 °C for 1 h. Then, the treated catalysts were cooled down to room temperature. Afterwards, the catalysts were exposed to a flow of 10 vol.% H_2/Ar (50 mL/min) and heated from 40 to 1000 °C linearly. The ramping rate was set at 10 °C/min. The signal of H_2 was monitored by a thermal conductivity detector (TCD).

NH_3-temperature-programmed desorption (NH_3-TPD) experiments were performed on a fixed-bed quartz tube reactor, using an online mass spectrometer (HPR20, Hiden Analytical Ltd., UK) as a detector. Prior to the test, samples were pretreated in a flow of 20 vol.% O_2/He (30 mL/min) at 300 °C for 30 min and then cooled to room temperature. After the pretreatment, samples were exposed to a flow with 2500 ppm NH_3/Ar to saturation. Afterwards, the samples were purged by N_2 flow for 30 min. Finally, the samples were heated to 600 °C, and the ramping rate was 10 °C/min. The m/z of 15 was used to identify NH_3.

An FTIR spectrometer (Nicolet Nexus 670, USA) equipped with an MCT/A detector was employed to conduct *in situ* diffuse reflectance infrared Fourier transform spectroscopy (*in situ* DRIFTS) experiments. Prior to the test, samples loaded in the DRIFTS cell were pretreated with air flow at 400 °C for 30 min. Then, the sample was cooled and kept at 150 °C, at which the background samples were also collected. The background spectra were subtracted from the recorded spectra automatically. The feeding gas was composed of 500 ppm NO (when used), 500 ppm NH_3 (when used) and 5 vol.% O_2 (when used), with a total flow rate of 300 min (N_2 balance). The range of all spectra was 400–4000 cm^{-1} and the spectral resolution was 4 cm^{-1}.

2.3 Catalytic performance evaluation

A fixed-bed reactor was used to evaluate the NH_3-SCR activity and NH_3/NO oxidation activity on the prepared samples. The feed gas contained 500 ppm NO/NH_3 (when used), 100 ppm SO_2 (when used), 5 vol.% O_2 and 5% H_2O (when used), N_2 in balanced. In each test, 0.6 mL catalyst (40–60 mesh) was loaded in a quartz tube. To achieve the gas hourly space velocity (GHSV) of 10000, 25000, 50000 and 100000 h^{-1}, the total flow rate was controlled at 100, 250, 500 and 1000 mL/min, respectively. An FTIR spectrometer (Nicolet Nexus 670, USA) with a multiple-path gas cell (2 m) was employed to measure the concentrations of NO, NO_2, N_2O and NH_3 in the outlet gas. The NO_x conversion in NH_3-SCR reaction was calculated according to the equation attached below (Eq. (1)):

$$NO_x \text{ conversion } (\%) = \{([NO]_{in} - [NO]_{out} - [NO_2]_{out})/[NO]_{in}\} \times 100\% \quad (1)$$

The NH_3 conversion in NH_3 oxidation reaction was determined by the following equation (Eq. (2)):

$$NH_3 \text{ conversion } (\%) = \{([NH_3]_{in} - [NH_3]_{out})/[NH_3]_{in}\} \times 100\% \quad (2)$$

The NO conversion in NO oxidation reaction was determined by the following equation (Eq. (3)):

$$NO \text{ conversion } (\%) = \{([NO]_{in} - [NO]_{out})/[NO]_{in}\} \times 100\% \quad (3)$$

3 Results and discussion

3.1 Catalytic activity

The catalytic activity on $FeCe_aTiO_x$ catalysts (a = 0.1, 0.2, 0.5, 1 and 1.6) in NH_3-SCR reaction was evaluated first. As the CeO_2 doping amount increased, the low-temperature (< 250 °C) NH_3-SCR activity on $FeCe_aTiO_x$ catalysts initially increased and then decreased (Fig. 1(a)). In this study, $FeCe_{0.2}TiO_x$ catalyst showed the best NH_3-SCR activity in the low-temperature range (150–250 °C), with a T_{90} (at which the NO_x conversion reached 90%) of 195 °C which was much lower than that on $FeTiO_x$ catalyst (T_{90} =

245 °C). It can be concluded that the doping of proper amount of CeO_2 could significantly boost the $DeNO_x$ efficiency of $FeTiO_x$ catalyst below 250 °C. Moreover, $FeCe_{0.2}TiO_x$ still exhibited a broad operation temperature window from 200 to 350 °C under higher GHSV such as 100000 h^{-1} (Fig. S1).

The deactivation of catalysts caused by SO_2 and H_2O in the flue gas is a bottleneck in industrial application of NH_3-SCR catalysts (Wang et al., 2020b). Here, the catalytic performance of $FeCe_{0.2}TiO_x$ with H_2O and/or SO_2 added to feed gas was evaluated. As illustrated in Fig. 1(b), water vapor (5 vol.%) in the reaction flow had no impact on the NH_3-SCR activity of $FeCe_{0.2}TiO_x$ catalyst. Only a slight decline in the NH_3-SCR activity was observed on $FeCe_{0.2}TiO_x$ after being exposed to 100 ppm SO_2 for 24 h, indicating the good SO_2 resistance of $FeCe_{0.2}TiO_x$ catalyst. Although the NO_x conversion on $FeCe_{0.2}TiO_x$ decreased with the addition of 5 vol.% H_2O and 100 ppm SO_2 to the reaction flow at the same time, which might result from the deposition and accumulation of ammonium bisulfate (ABS) on the catalyst surface that covered the active sites (Guo et al., 2019; Guo et al., 2021). Interestingly, the NO_x conversion was found to recover to *ca.* 100% rapidly after switching off SO_2 and H_2O, suggesting that the deactivated $FeCe_{0.2}TiO_x$ catalyst was easy to regenerate.

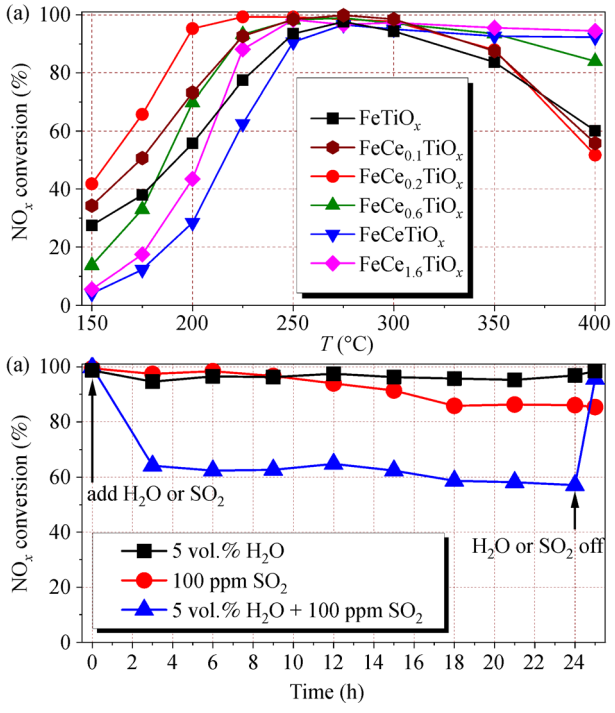

Fig. 1 (a) The NH_3-SCR activity over $FeTiO_x$ and $FeCe_aTiO_x$ catalysts (a = 0.1, 0.2, 0.6, 1 and 1.6) under GHSV of 50000 h^{-1}. (b) The NO_x conversion as a function of reaction time in NH_3-SCR reaction over $FeCe_{0.2}TiO_x$ catalyst in the presence of 100 ppm SO_2 or/and 5% H_2O at 250 °C under the GHSV of 50000 h^{-1}.

3.2 Structural information

The XRD patterns for $FeCe_aTiO_x$ catalysts are illustrated in Fig. 2(a). For $FeTiO_x$ catalyst, diffraction peaks ascribed to hematite α-Fe_2O_3 (JCPDS 33-0664), anatase TiO_2 (JCPDS 21-1272) and pseudobrookite Fe_2TiO_5 (JCPDS 41-1432) were observed. After the addition of CeO_2, the intensity of the diffraction peaks attributed to Fe_2O_3, TiO_2 and Fe_2TiO_5 decreased significantly, indicating the much lower crystallinity of Fe and Ti species. Interestingly, no formation of crystalline CeO_2 was observed on $FeCe_{0.1}TiO_x$ and $FeCe_{0.2}TiO_x$, which indicated that CeO_2 was highly dispersed within these two catalysts. When the CeO_2 doping amount was further increased, $FeCe_aTiO_x$ (a = 0.6, 1, 1.6) mainly showed a cerianite CeO_2 phase (JCPDS 43-1002) with monotonically increased diffraction peak intensity. It was noticeable that the intensity of diffraction peaks for $FeCe_{0.2}TiO_x$ catalyst was the lowest among all the catalysts, which was related to its lowest crystallinity and the smallest particle size. Accordingly, $FeCe_{0.2}TiO_x$ also showed the highest specific surface area (Table S1). $FeCe_{0.2}TiO_x$ catalyst with the smallest crystallite size and highest specific surface area could provide the most fruitful

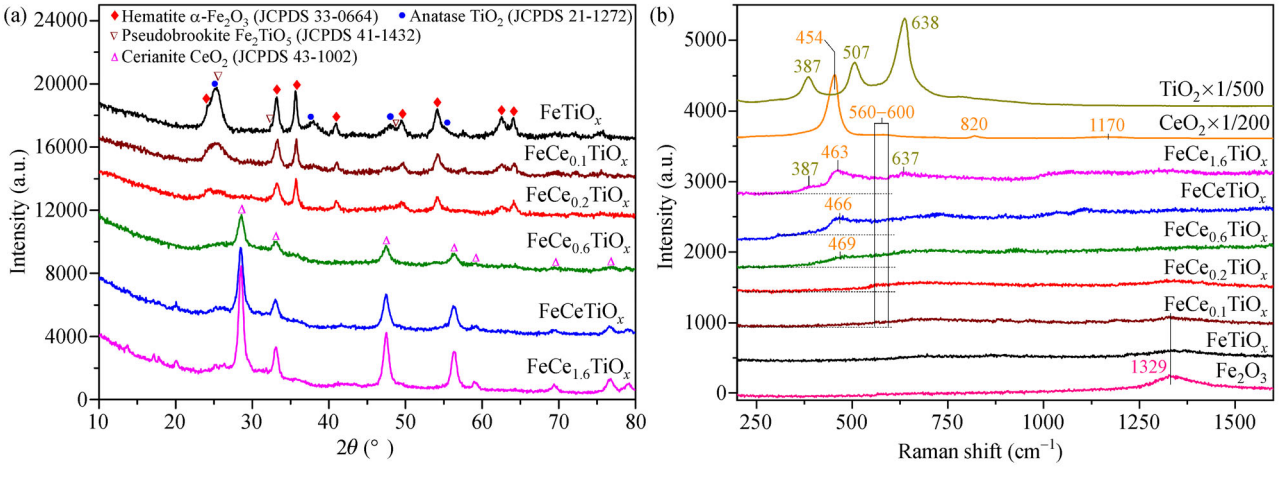

Fig. 2 (a) XRD patterns and (b) Raman spectra for $FeTiO_x$ and $FeCe_aTiO_x$ catalysts with reference oxides.

active sites among the studied catalysts herein to optimally impel the proceeding of the NH_3-SCR reaction.

Raman spectra of $FeCe_aTiO_x$ catalysts were also collected to further explain the catalyst structure (Fig. 2(b)). For TiO_2, three characteristic Raman active modes of anatase with symmetries B_{1g}, A_{1g} and E_g were observed at 387, 507, and 638 cm^{-1}, respectively (Challagulla et al., 2017). For pure CeO_2, an intensive band ascribed to the triply degenerated F_{2g} mode of fluorite-type CeO_2 could be observed at *ca.* 454 cm^{-1}, and the bands at *ca.* 560–600, 820 and 1170 cm^{-1} could be attributed to the oxygen defects (D-band, LO), peroxide species (O_2^{2-}) and superoxide species (O_2^-) on oxygen defects (2LO, overtone of the LO mode), respectively (Loridant, 2021). The band at *ca.* 1329 cm^{-1} on Fe_2O_3 was related to the characteristic signal of α-Fe_2O_3 (Ahmmad et al., 2013). For $FeCe_aTiO_x$ catalysts, the intensity of the Raman bands decreased significantly when compared with pristine Fe_2O_3, TiO_2 and CeO_2 within their respective characteristic Raman shift region, especially for $FeCe_{0.2}TiO_x$ catalyst on which only a broad band related to oxygen defect (*ca.* 560 cm^{-1}) was detected. The absence of typical Raman shifts observed for crystalline Fe_2O_3, CeO_2 and TiO_2 on $FeCe_{0.2}TiO_x$ well supported the results of XRD indicating that $FeCe_{0.2}TiO_x$ showed the lowest crystallinity. As reported previously, mixed oxide catalysts such as CeO_2-SiO_2 and $FeNbO_x$ with low crystallinity (or in totally amorphous state) could exhibit higher specific surface area, improved redox property and enhanced surface acidity comparing to one-component crystalline metal oxide, thus providing more active sites. The strong interaction of Ce-O-Si or Fe-O-Nb in such mixed oxides with low crystallinity played a key role in the dramatic improvement of the low-temperature NH_3-SCR activity (Tan et al., 2021a; Zhang et al., 2021a).

3.3 States of Fe and Ce species within $FeCe_aTiO_x$

To better understand the surface chemical states of $FeCe_aTiO_x$ catalysts, XPS measurements were conducted. The surface atomic concentration could be found in Table S2. Fe 2p XPS for Fe_2O_3, $FeTiO_x$ and $FeCe_{0.2}TiO_x$ are illustrated in Fig. S2(a). The high similarity of the Fe 2p XPS for these three samples indicated that the Fe species in $FeTiO_x$ and $FeCe_{0.2}TiO_x$ were both in the form of Fe^{3+} (Yu et al., 2021a). As demonstrated in Fig. S2(b), the intensity of Ce 3d XPS for $FeCe_{0.2}TiO_x$ was much weaker than that for CeO_2 due to its low Ce content. The surface Ce^{3+} concentration was calculated following the method reported elsewhere (Tan et al., 2020). The concentration of Ce^{3+} on $FeCe_{0.2}TiO_x$ (20.0%) was almost equal to that on CeO_2 (19.8%). The O 1s XPS were also collected and illustrated in Fig. S2(c). The peaks at *ca.* 534 and 531 eV (O_α) could be assigned to surface hydroxyl groups and chemisorbed oxygen species, respectively. The peak at *ca.* 530 eV (O_β) was related to the lattice oxygen species (Liu et al., 2018; Li et al., 2021). Interestingly, the ratio of surface oxygen species ($O_\alpha/(O_\alpha+O_\beta)$) on $FeCe_{0.2}TiO_x$ (42.8%) was higher than that on $FeTiO_x$ (38.5%), which might result from the higher specific surface area and lower crystallinity of $FeCe_{0.2}TiO_x$ (Table S2).

The XAFS technique (including XANES and EXAFS) was applied to further elucidate the chemical states of Fe and Ce species, as well as the microstructure of $FeCe_aTiO_x$ catalysts in detail. Figure 3(a) illustrated the Fe K-edge XANES of $FeCe_aTiO_x$ and the reference samples. Judging from the pre-edge peak position, it can be concluded that the Fe species in $FeTiO_x$ and $FeCe_aTiO_x$ mainly existed in the form of Fe^{3+}, which was well supported by our previous report (Liu et al., 2013) and the Fe 2p XPS results. In XRD and Raman spectra sections, it has been found that CeO_2 and Fe_2O_3 in $FeCe_{0.2}TiO_x$ showed low crystallinity, suggesting that Ce and Fe species were well mixed with each other. According to the EXAFS results (Fig. 3(b)), besides the well-defined Fe-O first coordination shell within Fe_2O_3, $FeTiO_x$ and $FeCe_aTiO_x$, a second coordination shell of Fe-O-M (M = Fe, Ce, Ti) was also observed on these samples. It was worth noting that the Fe-O coordination intensity on $FeCe_{0.2}TiO_x$ catalyst was the lowest among all Fe containing samples, indicating the formation of the most abundant unsaturated coordination sites for Fe species within this optimal catalyst.

To further investigate the formation of Fe-O-M structure in $FeCe_aTiO_x$ catalysts, Ce K-edge XANES and EXAFS were also collected and illustrated in Figs. 3(c) and 3(d). No significant difference regarding to absorption edge energy was observed for the Ce K-edge XANES of CeO_2 and $FeCe_aTiO_x$, suggesting that Ce in $FeCe_aTiO_x$ mainly existed in the form of Ce^{4+}. Interestingly, different from the EXAFS of CeO_2 in R space where well-defined Ce-O and Ce-O-Ce coordination shells were observed, no Ce-O-Ce coordination shell was found on $FeCe_{0.1}TiO_x$ and $FeCe_{0.2}TiO_x$ with relatively low Ce doping. The absence of the Ce-O-Ce coordination environment within $FeCe_{0.2}TiO_x$ catalyst clearly confirmed that CeO_2 was in a highly dispersed state. Moreover, a new coordination shell of Ce-O-Fe was formed within $FeCe_{0.1}TiO_x$ and $FeCe_{0.2}TiO_x$ as confirmed by curve fitting, suggesting the existence of strong interaction between Ce and Fe species. The electron transfer through such strong interaction within Ce-O-Fe could facilitate the redox cycle of active sites in NH_3-SCR reaction, thus contributing to the improvement of the low-temperature NH_3-SCR activity.

3.4 Surface acidity and redox property

As widely reported, NH_3-SCR reaction requires two types of active sites, i.e., the redox sites and acid sites, which jointly determine the catalytic performance of a specific NH_3-SCR catalyst (Han et al., 2019; Tan et al., 2021b). In this study, NH_3-TPD was first conducted to explore the surface acidity of $FeTiO_x$ and $FeCe_{0.2}TiO_x$ catalysts. As

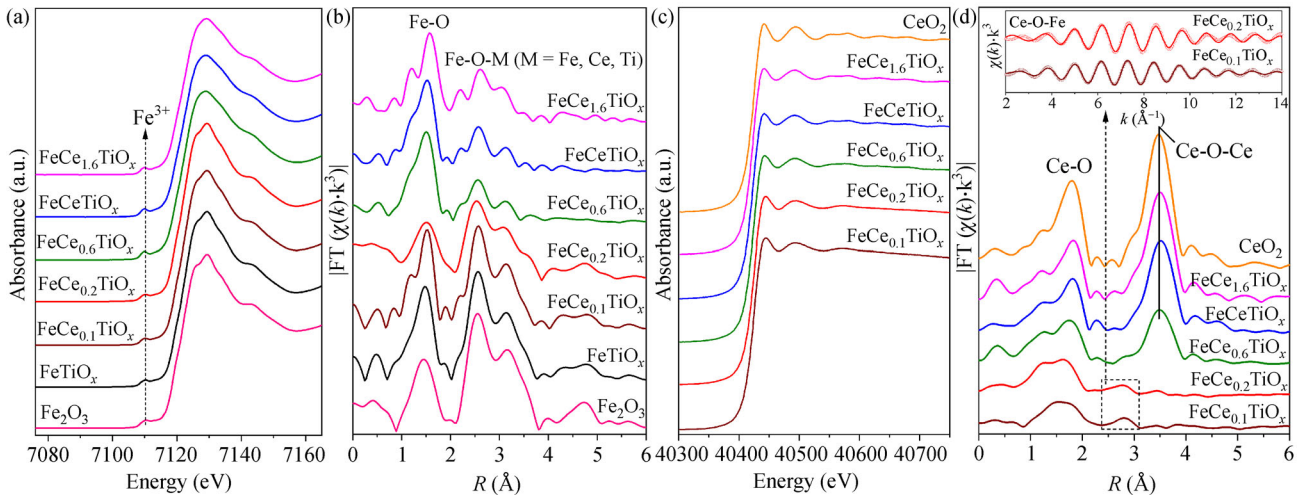

Fig. 3 (a) Normalized XANES spectra of Fe K-edge in Fe_2O_3, $FeTiO_x$ and $FeCe_aTiO_x$ catalysts, (b) Fourier transforms of filtered EXAFS oscillations $k^3\chi(k)$ into R space for Fe K-edge in Fe_2O_3, $FeTiO_x$ and $FeCe_aTiO_x$ catalysts. (c) Normalized XANES spectra of Ce K-edge in CeO_2 and $FeCe_aTiO_x$ catalysts, (d) Fourier transforms of filtered EXAFS oscillations $k^3\chi(k)$ into R space for Ce K-edge in CeO_2 and $FeCe_aTiO_x$ catalysts (the inserted figure was the inverse Fourier transformed EXAFS oscillations in $FeCe_{0.1}TiO_x$ and $FeCe_{0.2}TiO_x$ in the R range of *ca.* 2.3–3.2 Å, in which the dotted lines were related to the calculated EXAFS oscillations of Ce-O-Fe bond using FEFF8.4 code)。

illustrated in Fig. 4(a), the NH_3-TPD profile for $FeCe_{0.2}TiO_x$ showed no significant difference from that for $FeTiO_x$. Only a slight increase in the NH_3 adsorption amount was observed on $FeCe_{0.2}TiO_x$, which might be due to its higher specific surface area. *In situ* DRIFTS of NH_3 adsorption was performed to further explore the characteristics of NH_3 adsorption on $FeTiO_x$ and $FeCe_{0.2}TiO_x$ at 150 °C (Fig. 4(b)). IR bands related to NH_3 adsorbed on Lewis acid sites (1184–1192 and 1603 cm^{-1}) and Brønsted acid sites (1446–1462 and 1680 cm^{-1}) were observed on both $FeTiO_x$ and $FeCe_{0.2}TiO_x$ (Yao et al., 2017; Yu et al., 2021b). The IR spectra for NH_3 adsorption on $FeTiO_x$ and $FeCe_{0.2}TiO_x$ were almost the same, indicating that the surface acidity did not dominate the NH_3-SCR activity difference on these two catalysts. However, interestingly, a weak band assigned to -NH_2 species at 1531 cm^{-1} was observed on $FeCe_{0.2}TiO_x$, which was formed by the oxidative dehydrogenation of NH_3 on Lewis acid sites (Liu et al., 2014). The formation of -NH_2 species indicated the better redox property of $FeCe_{0.2}TiO_x$, which could be a decisive factor for the enhancement of low-temperature NO_x elimination efficiency. The higher NH_3 oxidation activity on $FeCe_{0.2}TiO_x$ comparing to that on $FeTiO_x$ further supported the viewpoint that $FeCe_{0.2}TiO_x$ catalyst could better activate NH_3 (Fig. S3(a)).

To study the redox property and reveal the structural

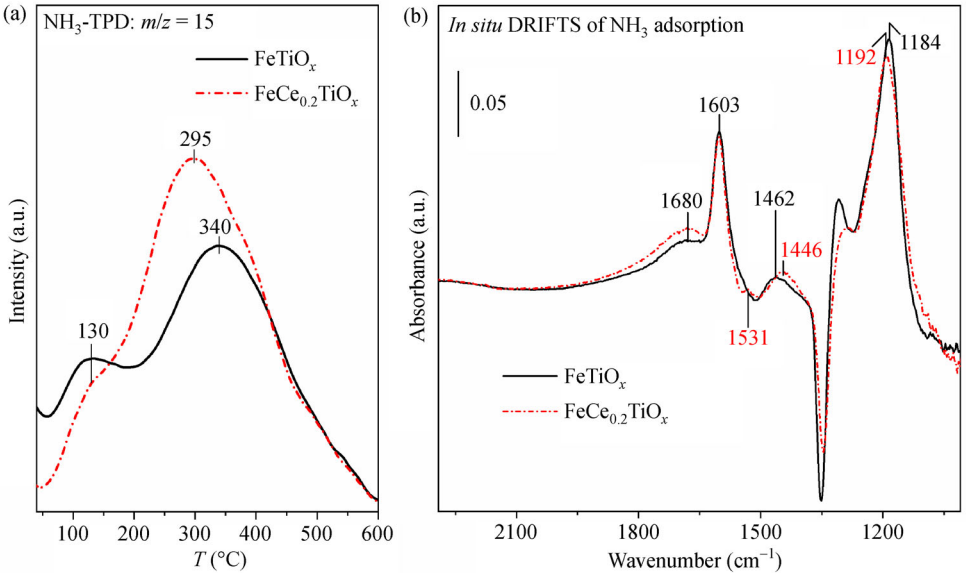

Fig. 4 (a) NH_3-TPD profiles for $FeTiO_x$ and $FeCe_{0.2}TiO_x$ catalysts; (b) *In situ* DRIFTS of NH_3 adsorption on $FeTiO_x$ and $FeCe_{0.2}TiO_x$ catalysts at 150 °C collected in N_2 flow.

information of the prepared catalysts, H_2-TPR profiles of the prepared samples were collected and further peak deconvolution was conducted (Fig. 5). Three sets of H_2-consumption peaks at *ca.* 200–350 °C (black), *ca.* 350–500 °C (red) and *ca.* 500–900 °C (blue) could be attributed to the reduction of Fe^{3+} (similar to the Fe species in Fe_2O_3) to $Fe^{2+/3+}$ (similar to the Fe species in Fe_3O_4), Fe^{2+} (similar to the Fe species in FeO) and metallic Fe^0, respectively (Qu et al., 2015). As listed in Table S3, although the total H_2 consumption of $FeTiO_x$ and $FeCe_{0.2}TiO_x$ was much smaller than that of Fe_2O_3, which should be related to the poor reducibility of TiO_2, higher ratio of H_2 consumption occurred at low temperatures (200–350 °C) for $FeCe_{0.2}TiO_x$ (25.3%) when compared with those for Fe_2O_3 (12.8%) and $FeTiO_x$ (18.1%), suggesting that the reduction of Fe^{3+} to Fe^{2+} was much easier on $FeCe_{0.2}TiO_x$ catalyst. Such improved reducibility suggested the key role of CeO_2 doping in tuning the redox property of $FeCe_{0.2}TiO_x$ catalyst.

To further investigate the reduction process of $FeTiO_x$ and $FeCe_{0.2}TiO_x$ in H_2 flow, *in situ* Fe-K XAFS during the H_2-TPR experiments were measured using quick XAS method (Fig. 6). As shown by the absorption edge shift (inserted figures in Figs. 6(a) and 6(b)) and the post-edge pattern change in the *in situ* Fe-K XANES results, during the H_2 reduction process, the Fe species within $FeCe_{0.2}$-TiO_x catalyst could be gradually reduced into different valence states at much lower temperatures than those within $FeTiO_x$ catalyst. Based on the detailed comparison of Fe-K EXAFS at different reduction temperatures, the reducibility of Fe species within these two catalysts could be clearly differentiated (Figs. 6(c) and 6(d)). For both $FeTiO_x$ and $FeCe_{0.2}TiO_x$ catalysts, the reduction procedure of Fe species could be divided into three steps. Consistent with Fe 2p XPS results, the valence of Fe species in $FeTiO_x$ was +3. When the reduction temperature reached 350 °C, Fe^{3+} species in $FeTiO_x$ were reduced to $Fe^{2+/3+}$ (similar to the Fe species in Fe_3O_4). Afterwards, $Fe^{2+/3+}$ species could be further converted into Fe^{2+} (similar to the Fe species in FeO) and metallic Fe^0 at *ca.* 500 °C and 900 °C, respectively. Such three-stage reduction procedure could be represented as $Fe^{3+} \rightarrow Fe^{2+/3+} \rightarrow Fe^{2+} \rightarrow Fe^0$, which further supported the viewpoint proposed in the H_2-TPR section. It should be noted that the Fe^{3+} species within $FeCe_{0.2}TiO_x$ could be reduced into $Fe^{2+/3+}$ at 300 °C, which was much lower than the corresponding required reduction temperature of $FeTiO_x$ (350 °C). Moreover, the *in situ* formed $Fe^{2+/3+}$ species within $FeCe_{0.2}TiO_x$ could be further reduced into Fe^{2+} at 450 °C, 50 °C lower than that within $FeTiO_x$ as well. The much lower reduction temperature of Fe species on $FeCe_{0.2}TiO_x$ indicated that the Ce doping could effectively improve its redox property at low temperatures. Considering the formation of Ce-O-Fe structure within $FeCe_{0.2}TiO_x$, the better reducibility of Fe^{3+} could facilitate the redox cycle of $Fe^{3+} + Ce^{3+} \leftrightarrow Fe^{2+} + Ce^{4+}$, which might boost the NH_3-SCR activity on $FeCe_{0.2}TiO_x$ catalyst, especially in the low-temperature range. Moreover, the enhanced NO oxidation activity on $FeCe_{0.2}TiO_x$ also supported the viewpoint that CeO_2 doping would improve the redox properties of $FeTiO_x$ (Fig. S3(b)).

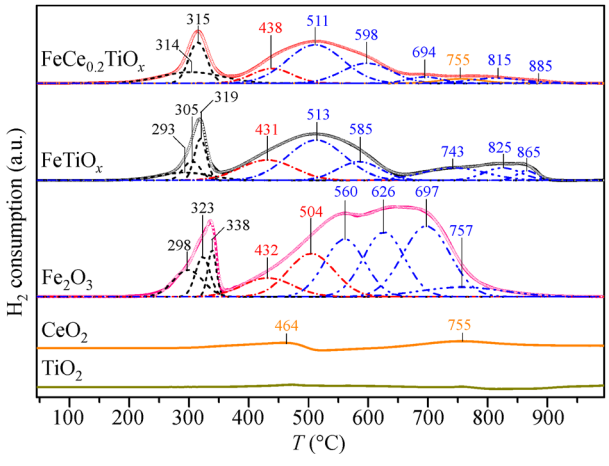

Fig. 5 H_2-TPR profiles for $FeTiO_x$ and $FeCe_{0.2}TiO_x$ catalysts, with TiO_2, CeO_2 and Fe_2O_3 as reference samples.

3.5 Reaction mechanism

Systematic *in situ* DRIFTS experiments were conducted to explore the NH_3-SCR reaction mechanism on $FeTiO_x$ and $FeCe_{0.2}TiO_x$ catalysts. As illustrated in Fig. 7(a), with the introduction of $NO + O_2$ to the gas cell, NH_3 species pre-adsorbed on both Lewis acid sites (1186, 1603, 3157, 3261 and 3354 cm^{-1}) and Brønsted acid sites (1464 and 1684 cm^{-1}) (Peng et al., 2013; Ma et al., 2016) could be consumed rapidly on $FeTiO_x$ catalyst, indicating that the pre-adsorbed NH_3 species were highly reactive in NH_3-SCR reaction. As the reaction time increased, several new bands assigned to adsorbed NO_x emerged. The bands at *ca.* 1545 and 1242 cm^{-1} could be assigned to monodentate nitrate species, and the formation of bridging nitrates (*ca.* 1606 cm^{-1}) and bidentate nitrates (*ca.* 1583 cm^{-1}) was also observed (Yao et al., 2017). The negative bands at *ca.* 1352, 3649, 3691 and 3714 cm^{-1} were related to the consumption of surface hydroxyl groups (Ma et al., 2015). The reactivity of surface adsorbed NO_x species was also evaluated on $FeTiO_x$ catalyst (Fig. 7(b)). With the introduction of NH_3 to $FeTiO_x$ catalyst pre-adsorbed with NO_x, besides the bands assigned to adsorbed NH_3 species on Lewis acid sites (1196, 1603, 3155, 3261 and 3356 cm^{-1}) or Brønsted acid sites (1471 and 1684 cm^{-1}), several new bands attributed to surface ammonium nitrates (NH_4NO_3) emerged at *ca.* 1261, 1284 and 1523 cm^{-1} (Liu and He, 2010). However, no obvious decomposition of the deposited NH_4NO_3 was observed in 60 min, indicating that the reaction between NH_3 and adsorbed NO_x was not the main pathway on $FeTiO_x$ catalysts. When the NH_3-SCR

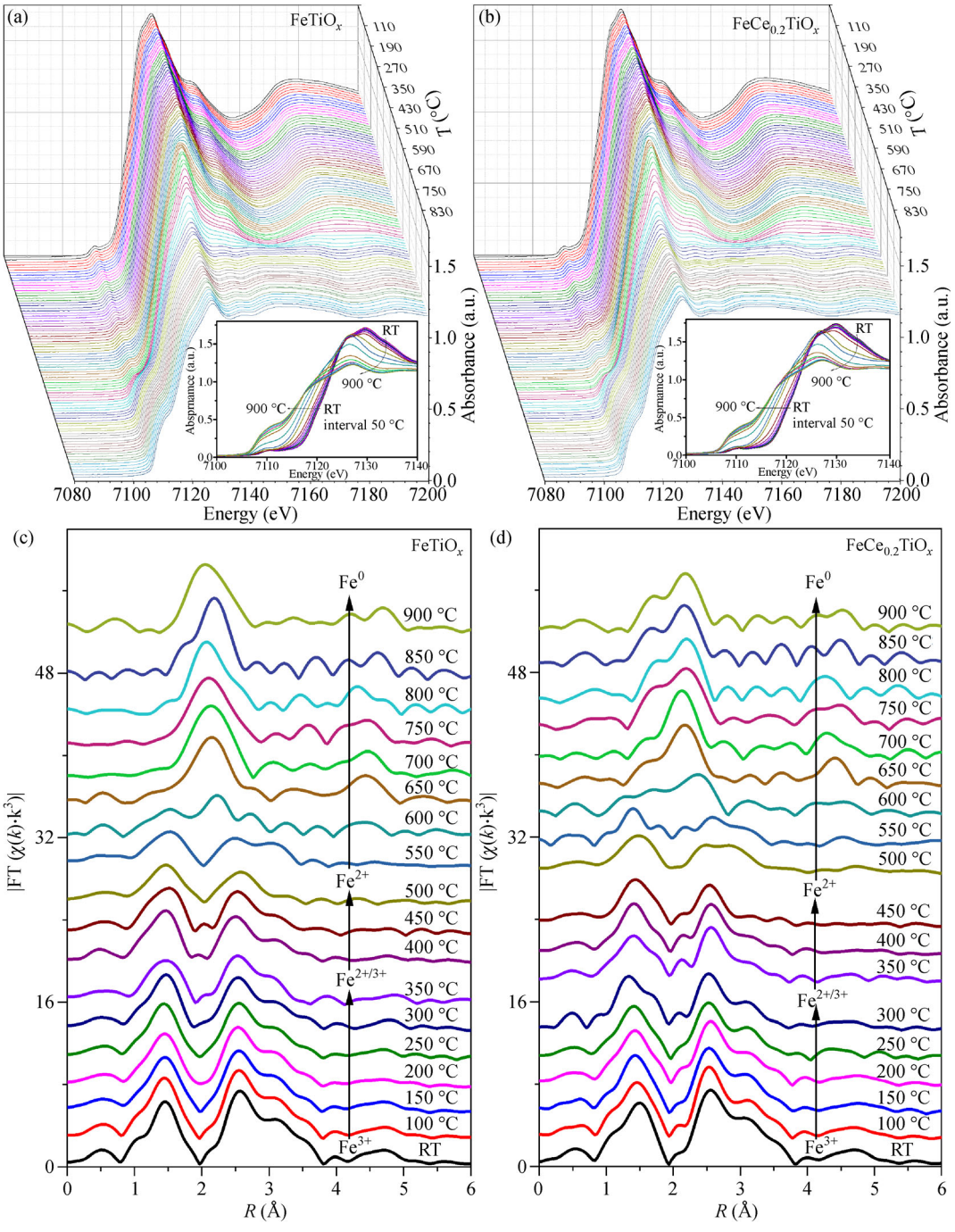

Fig. 6 The normalized *in situ* Fe K-edge XANES for (a) $FeTiO_x$ and (b) $FeCe_{0.2}TiO_x$ catalysts in the H_2-TPR process from room temperature to 900°C (the inserted figures showed the normalized *in situ* Fe K-edge XANES with an interval of 50°C for better discrimination); *In situ* EXAFS spectra of Fe K-edge for (c) $FeTiO_x$ and (d) $FeCe_{0.2}TiO_x$ catalysts during the H_2-TPR process.

reaction flow (NH_3 + NO + O_2) was introduced onto $FeTiO_x$ (Fig. 7(c)), the bands assigned to NH_3 species bound to Lewis acid sites and Brønsted acid sites were observed. As for the adsorbed NO_x species, only a weak band at *ca.* 1572 cm^{-1} attributed to bidentate nitrates was detected. Moreover, the deposition of NH_4NO_3 was inhibited under the NH_3-SCR reaction condition. It can be concluded that the NH_3-SCR reaction on $FeTiO_x$ catalyst mainly followed an Eley-Rideal (E-R) reaction pathway at the investigated temperature.

As discussed above, the NH_3 adsorption on $FeCe_{0.2}TiO_x$ was very similar to that on $FeTiO_x$. When NO + O_2 flow was introduced onto $FeCe_{0.2}TiO_x$ pre-adsorbed with NH_3, adsorbed NH_3 species were consumed by NO + O_2 rapidly, suggesting that the NH_3-SCR reaction on $FeCe_{0.2}TiO_x$ could proceed through the E-R reaction pathway efficiently (Fig. 8(a)). As shown in Fig. 8(b), it was also found that abundant NH_4NO_3 species (1257,

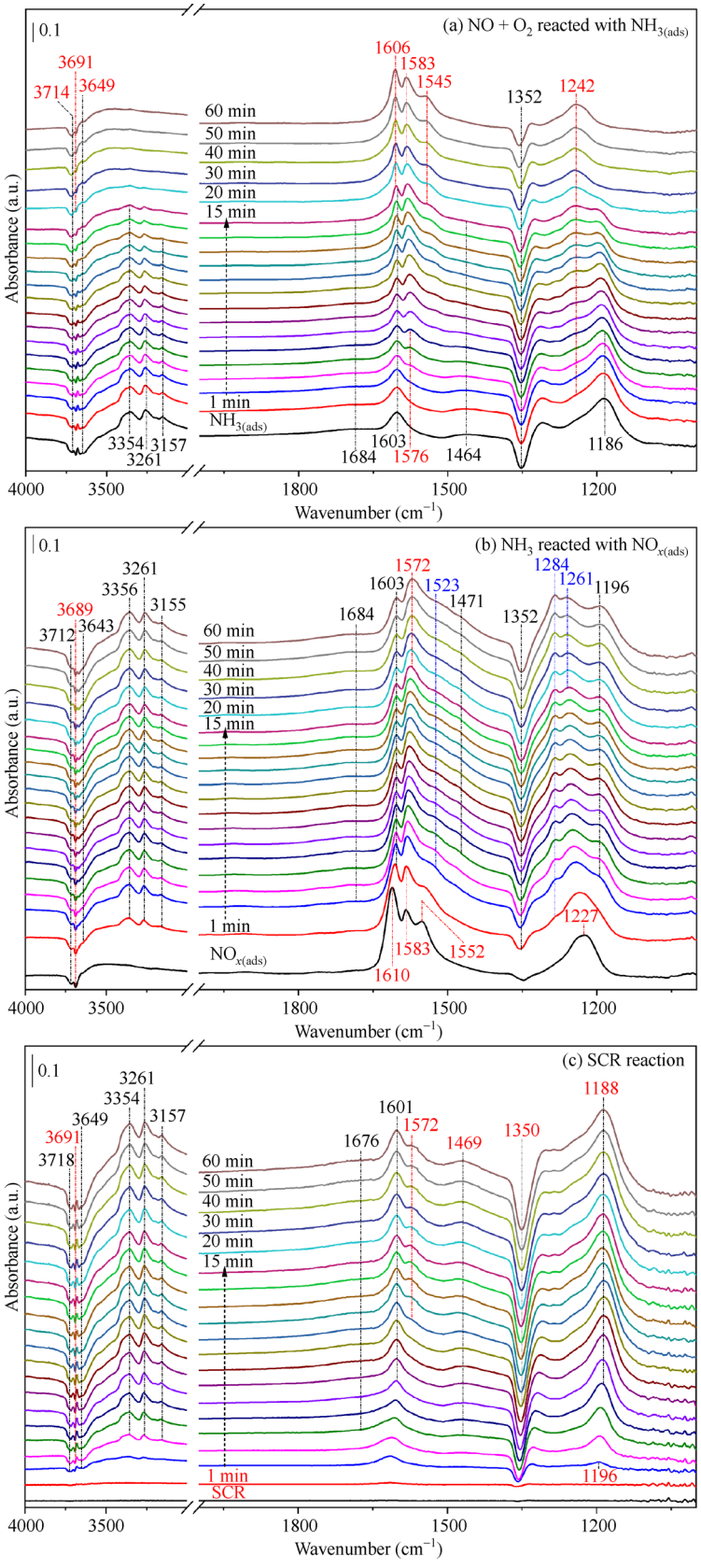

Fig. 7 *In situ* DRIFTS of (a) NO + O_2 reacting with pre-adsorbed NH_3 species; (b) NH_3 reacting with pre-adsorbed NO_x species; (c) NH_3-SCR reaction at 150 °C over $FeTiO_x$. The FTIR spectra were collected in varied reactant flow according to the needs of the experiments.

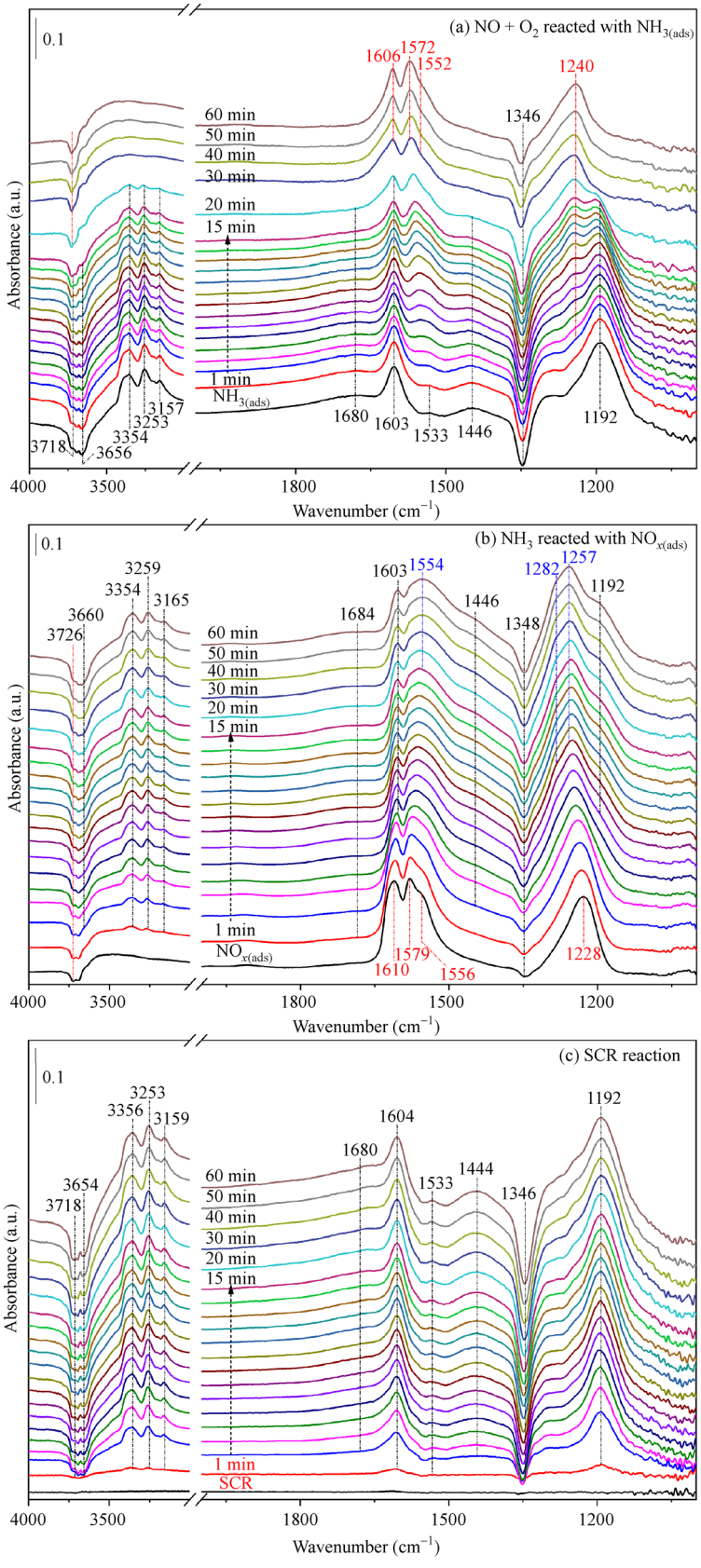

Fig. 8 *In situ* DRIFTS of (a) NO + O_2 reacting with pre-adsorbed NH_3 species; (b) NH_3 reacting with pre-adsorbed NO_x species; (c) NH_3-SCR reaction at 150 °C over $FeCe_{0.2}TiO_x$. The FTIR spectra were collected in varied reactant flow according to the needs of the experiments.

1282 and 1554 cm^{-1}) were formed during the reaction between NH_3 and pre-adsorbed NO_x on $FeCe_{0.2}TiO_x$. The accumulation of NH_4NO_3 species without further decomposition to N_2 and H_2O at the investigated temperature was not the main reason for the improvement of low-temperature NH_3-SCR activity on $FeCe_{0.2}TiO_x$ catalyst. When the NH_3-SCR reaction flow was introduced to the DRIFTS cell, no obvious bands assigned to nitrate species or NH_4NO_3 species were detected on $FeCe_{0.2}TiO_x$ (Fig. 8(c)). Besides the bands assigned to NH_3 species bound to acid sites and the consumed hydroxyl groups, the additional -NH_2 species (*ca.* 1533 cm^{-1}) could be detected throughout the NH_3-SCR process. Such -NH_2 species originated from the oxidative dehydrogenation of NH_3 could directly react with gaseous NO forming NH_2NO. The generated NH_2NO could easily decompose into N_2 and H_2O at low temperatures (Li and Li, 2014; Zhu et al., 2017). The facile formation of -NH_2 species on $FeCe_{0.2}TiO_x$ surface was the main reason for its superior low-temperature $DeNO_x$ efficiency comparing to $FeTiO_x$.

To better demonstrate the difference between the surface adsorbed species and their reactivity on $FeTiO_x$ and $FeCe_{0.2}TiO_x$, the *in situ* DRIFTS results of NH_3-SCR reaction under steady-state on these two catalysts at 150 °C was illustrated comparatively in Fig. 9(a). Although the profiles for *in situ* DRIFTS of NH_3 or NO_x adsorption on $FeTiO_x$ and $FeCe_{0.2}TiO_x$ at 150 °C were similar (Figs. 4(b) and S4), especially for the intensity of the bands assigned to NH_3 bound to surface acid sites, much lower intensity of the bands assigned to the adsorbed NH_3 species on the Lewis acid sites was observed on $FeCe_{0.2}TiO_x$ (1192 and 1604 cm^{-1}) under the steady-state NH_3-SCR reaction condition. This result clearly suggests that much faster consumption rate of adsorbed NH_3 species could be achieved on $FeCe_{0.2}TiO_x$ catalyst at the low temperature of 150 °C. Significantly, the presence of -NH_2 species (1533 cm^{-1}) indicates again that the facile activation of NH_3 was present on $FeCe_{0.2}TiO_x$, and the efficient reaction between -NH_2 and gaseous NO was responsible for the boosted NH_3-SCR activity at low temperatures. The reaction pathway on $FeTiO_x$ and $FeCe_{0.2}TiO_x$ was also demonstrated in Fig. 9(b).

4 Conclusions

CeO_2 doping is a simple strategy to promote the low-temperature $DeNO_x$ efficiency of $FeTiO_x$ catalyst, and a well improved $DeNO_x$ efficiency can be achieved on $FeCe_{0.2}TiO_x$ below 250 °C. $FeCe_{0.2}TiO_x$ catalyst exhibited a much lower crystallinity and higher specific surface area comparing to the $FeTiO_x$ counterpart. The systematic XAFS analysis revealed that the doped CeO_2 in $FeCe_{0.2}TiO_x$ was well mixed with Fe species, with the formation of abundant Ce-O-Fe microstructures. Such unique Ce-O-Fe microstructure dramatically improved the low-temperature redox property of $FeCe_{0.2}TiO_x$ catalyst, which triggered the facile activation of adsorbed NH_3 to form highly reactive -NH_2 species, thus promoting the low-temperature NH_3-SCR activity significantly. This work deepened the understanding of the origin of low-temperature $DeNO_x$ activity on CeO_2 doped $FeTiO_x$ catalyst and provided new guidance for the design of high-efficiency catalysts for NO_x elimination.

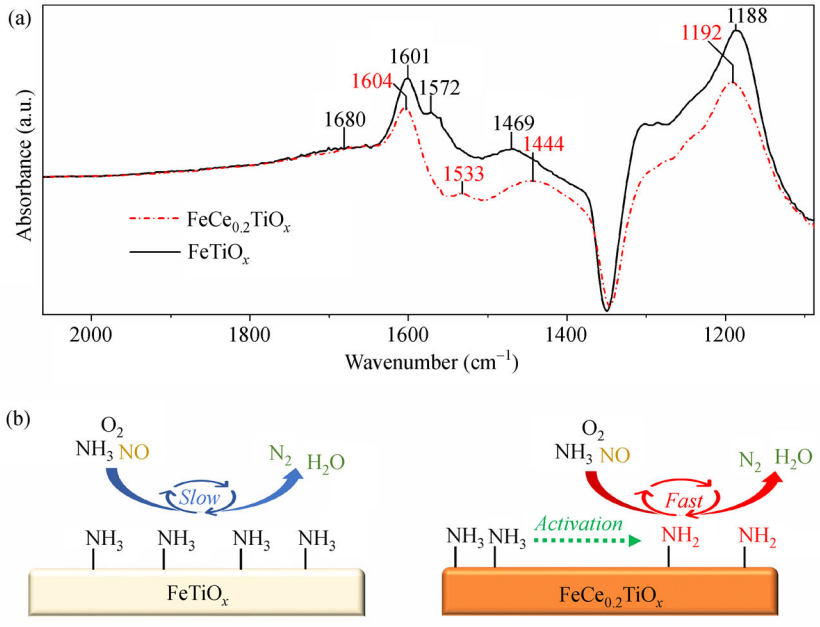

Fig. 9 (a) *In situ* DRIFTS of NH_3-SCR reaction on $FeTiO_x$ and $FeCe_{0.2}TiO_x$ at 150 °C collected in the NH_3-SCR reaction flow. (b) The scheme of the reaction pathway on $FeTiO_x$ and $FeCe_{0.2}TiO_x$ at 150 °C.

Acknowledgements F. L. acknowledges Startup Fund from the University of Central Florida (UCF) (USA). S. X. acknowledges the support from the Preeminent Postdoctoral Program (P3) at UCF (USA). H. H. acknowledges the support from the Key Project of National Natural Science Foundation of China (No. 21637005). The authors sincerely thank Prof. Kiyotaka Asakura from Hokkaido University (Japan) and Dr. Yasuhiro Niwa from Institute of Materials Structure Science (IMSS), High Energy Accelerator Research Organization (KEK) (Japan) for the generous help in XAS experiments conducted at Photon Factory, KEK, Japan (No. 2012G537).

Electronic Supplementary Material Supplementary material is available in the online version of this article at https://doi.org/10.1007/s11783-022-1539-2 and is accessible for authorized users.

References

Ahmmad B, Leonard K, Shariful Islam M, Kurawaki J, Muruganandham M, Ohkubo T, Kuroda Y (2013). Green synthesis of mesoporous hematite (α-Fe_2O_3) nanoparticles and their photocatalytic activity. Advanced Powder Technology, 24(1): 160–167

Ankudinov A L, Ravel B, Rehr J, Conradson S (1998). Real-space multiple-scattering calculation and interpretation of x-ray-absorption near-edge structure. Physical Review. B, 58(12): 7565–7576

Challagulla S, Tarafder K, Ganesan R, Roy S (2017). Structure sensitive photocatalytic reduction of nitroarenes over TiO_2. Scientific Reports, 7(1): 8783–8793

Chen Q, Zhang X, Li B, Niu S, Zhao G, Wang D, Peng Y, Li J, Lu C, Crittenden J (2021). Insight into the promotion mechanism of activated carbon on the monolithic honeycomb red mud catalyst for selective catalytic reduction of NO_x. Frontiers of Environmental Science & Engineering, 15(5): 92

Cook J W Jr, Sayers D E (1981). Criteria for automatic x‐ray absorption fine structure background removal. Journal of Applied Physics, 52(8): 5024–5031

Gan L, Li K, Niu H, Peng Y, Chen J, Huang Y, Li J (2021). Simultaneous removal of NO_x and chlorobenzene on V_2O_5/TiO_2 granular catalyst: Kinetic study and performance prediction. Frontiers of Environmental Science & Engineering, 15(4): 70

Guo K, Fan G, Gu D, Yu S, Ma K, Liu A, Tan W, Wang J, Du X, Zou W, Tang C, Dong L (2019). Pore size expansion accelerates ammonium bisulfate decomposition for improved sulfur resistance in low-temperature NH_3-SCR. ACS Applied Materials & Interfaces, 11(5): 4900–4907

Guo K, Ji J, Song W, Sun J, Tang C, Dong L (2021). Conquering ammonium bisulfate poison over low-temperature NH_3-SCR catalysts: A critical review. Applied Catalysis B: Environmental, 297: 120388–120403

Han L, Cai S, Gao M, Hasegawa J Y, Wang P, Zhang J, Shi L, Zhang D (2019). Selective catalytic reduction of NO_x with NH_3 by using novel catalysts: State of the art and future prospects. Chemical Reviews, 119(19): 10916–10976

He K, Huo H, Zhang Q (2002). Urban air pollution in China: Current status, characteristics, and progress. Annual Review of Energy and the Environment, 27(1): 397–431

Inomata Y, Kubota H, Hata S, Kiyonaga E, Morita K, Yoshida K, Sakaguchi N, Toyao T, Shimizu K I, Ishikawa S, Ueda W, Haruta M, Murayama T (2021). Bulk tungsten-substituted vanadium oxide for low-temperature NO_x removal in the presence of water. Nature Communications, 12(1): 557–567

Ji J, Jing M, Wang X, Tan W, Guo K, Li L, Wang X, Song W, Cheng L, Sun J, Song W, Tang C, Liu J, Dong L (2021). Activating low-temperature NH_3-SCR catalyst by breaking the strong interface between acid and redox sites: A case of model $Ce_2(SO_4)_3$-CeO_2 study. Journal of Catalysis, 399: 212–223

Kwon D W, Kim D H, Lee S, Kim J, Ha H P (2021). A dual catalytic strategy by the nature of the functionalization effect as well as active species on vanadium-based catalyst for enhanced low temperature SCR. Applied Catalysis B: Environmental, 289: 120032–120049

Lee K J, Kumar P A, Maqbool M S, Rao K N, Song K H, Ha H P (2013). Ceria added Sb-V_2O_5/TiO_2 catalysts for low temperature NH_3-SCR: Physico-chemical properties and catalytic activity. Applied Catalysis B: Environmental, 142–143: 705–717

Li W, Liu H, Chen Y (2017). Promotion of transition metal oxides on the NH_3-SCR performance of ZrO_2-CeO_2 catalyst. Frontiers of Environmental Science & Engineering, 11(2): 6

Li X, Li Y (2014). Molybdenum modified $CeAlO_x$ catalyst for the selective catalytic reduction of NO with NH_3. Journal of Molecular Catalysis A Chemical, 386: 69–77

Li Z, Dai S, Ma L, Qu Z, Yan N, Li J (2021). Synergistic interaction and mechanistic evaluation of NO oxidation catalysis on Pt/Fe_2O_3 cubes. Chemical Engineering Journal, 413: 127447–127455

Liu F, He H (2010). Selective catalytic reduction of NO with NH_3 over manganese substituted iron titanate catalyst: Reaction mechanism and H_2O/SO_2 inhibition mechanism study. Catalysis Today, 153(3–4): 70–76

Liu F, He H, Xie L (2013). XAFS study on the specific deoxidation behavior of iron titanate catalyst for the selective catalytic reduction of NO_x with NH_3. ChemCatChem, 5(12): 3760–3769

Liu F, He H, Zhang C (2008). Novel iron titanate catalyst for the selective catalytic reduction of NO with NH_3 in the medium temperature range. Chemical Communications, 17: 2043–2045

Liu F, He H, Zhang C, Feng Z, Zheng L, Xie Y, Hu T (2010). Selective catalytic reduction of NO with NH_3 over iron titanate catalyst: Catalytic performance and characterization. Applied Catalysis B: Environmental, 96(3–4): 408–420

Liu F, Shan W, Lian Z, Liu J, He H (2018). The smart surface modification of Fe_2O_3 by WO_x for significantly promoting the selective catalytic reduction of NO_x with NH_3. Applied Catalysis B: Environmental, 230: 165–176

Liu Z, Zhang S, Li J, Ma L (2014). Promoting effect of MoO_3 on the NO_x reduction by NH_3 over CeO_2/TiO_2 catalyst studied with *in situ* DRIFTS. Applied Catalysis B: Environmental, 144: 90–95

Loridant S (2021). Raman spectroscopy as a powerful tool to characterize ceria-based catalysts. Catalysis Today, 373: 98–111

Ma Z, Wu X, Härelind H, Weng D, Wang B, Si Z (2016). NH_3-SCR reaction mechanisms of $NbO_x/Ce_{0.75}Zr_{0.25}O_2$ catalyst: DRIFTS and kinetics studies. Journal of Molecular Catalysis A Chemical, 423: 172–180

Ma Z, Wu X, Si Z, Weng D, Ma J, Xu T (2015). Impacts of niobia loading on active sites and surface acidity in NbO_x/CeO_2-ZrO_2 NH_3-SCR catalysts. Applied Catalysis B: Environmental, 179: 380–394

Peng Y, Li K, Li J (2013). Identification of the active sites on CeO_2-WO_3 catalysts for SCR of NO_x with NH_3: An *in situ* IR and Raman

spectroscopy study. Applied Catalysis B: Environmental, 140– 141: 483–492

Qi G, Yang R T (2003). Performance and kinetics study for low-temperature SCR of NO with NH_3 over MnO_x-CeO_2 catalyst. Journal of Catalysis, 217(2): 434–441

Qu Z, Miao L, Wang H, Fu Q (2015). Highly dispersed Fe_2O_3 on carbon nanotubes for low-temperature selective catalytic reduction of NO with NH_3. Chemical Communications, 51(5): 956–958

Tan W, Liu A, Xie S, Yan Y, Shaw T E, Pu Y, Guo K, Li L, Yu S, Gao F, Liu F, Dong L (2021a). Ce-Si mixed oxide: A high sulfur resistant catalyst in the NH_3-SCR reaction through the mechanism-enhanced process. Environmental Science & Technology, 55(6): 4017–4026

Tan W, Wang C, Yu S, Li Y, Xie S, Gao F, Dong L, Liu F (2021b). Revealing the effect of paired redox-acid sites on metal oxide catalysts for efficient NO_x removal by NH_3-SCR. Journal of Hazardous Materials, 416: 125826–125836

Tan W, Wang J, Cai Y, Li L, Xie S, Gao F, Liu F, Dong L (2021c). Molybdenum oxide as an efficient promoter to enhance the NH_3-SCR performance of CeO_2-SiO_2 catalyst for NO_x removal. Catalysis Today, doi: 10.1016/j.cattod.2021.07.007

Tan W, Wang J, Li L, Liu A, Song G, Guo K, Luo Y, Liu F, Gao F, Dong L (2020). Gas phase sulfation of ceria-zirconia solid solutions for generating highly efficient and SO_2 resistant NH_3-SCR catalysts for NO removal. Journal of Hazardous Materials, 388: 121729–121740

Tang C, Zhang H, Dong L (2016). Ceria-based catalysts for low-temperature selective catalytic reduction of NO with NH_3. Catalysis Science & Technology, 6(5): 1248–1264

Wang J, Peng Z, Qiao H, Yu H, Hu Y, Chang L, Bao W (2016). Cerium-stabilized Cu-SSZ-13 catalyst for the catalytic removal of NO_x by NH_3. Industrial & Engineering Chemistry Research, 55(5): 1174–1182

Wang Y, Li G, Zhang S, Zhang X, Zhang X, Hao Z (2020a). Promoting effect of Ce and Mn addition on Cu-SSZ-39 zeolites for NH_3-SCR reaction: Activity, hydrothermal stability, and mechanism study. Chemical Engineering Journal, 393: 124782–124794

Wang Y, Yi W, Yu J, Zeng J, Chang H (2020b). Novel methods for assessing the SO_2 poisoning effect and thermal regeneration possibility of MO_x-WO_3/TiO_2 (M = Fe, Mn, Cu, and V) Catalysts for NH_3-SCR. Environmental Science & Technology, 54(19): 12612–12620

Yao X, Zhao R, Chen L, Du J, Tao C, Yang F, Dong L (2017). Selective catalytic reduction of NO_x by NH_3 over CeO_2 supported on TiO_2: Comparison of anatase, brookite, and rutile. Applied Catalysis B: Environmental, 208: 82–93

Yu Y, Tan W, An D, Tang C, Zou W, Ge C, Tong Q, Gao F, Sun J, Dong L (2021a). Activity enhancement of WO_3 modified $FeTiO_x$ catalysts for the selective catalytic reduction of NO_x by NH_3. Catalysis Today, 375: 614–622

Yu Y, Tan W, An D, Wang X, Liu A, Zou W, Tang C, Ge C, Tong Q, Sun J, Dong L (2021b). Insight into the SO_2 resistance mechanism on γ-Fe_2O_3 catalyst in NH_3-SCR reaction: A collaborated experimental and DFT study. Applied Catalysis B: Environmental, 281–291: 119544

Zeng Y, Haw K G, Wang Y, Zhang S, Wang Z, Zhong Q, Kawi S (2021). Recent progress of CeO_2-TiO_2 based catalysts for selective catalytic reduction of NO_x by NH_3. ChemCatChem, 13(2): 491–505

Zhang W, Shi X, Shan Y, Liu J, Xu G, Du J, Yan Z, Yu Y, He H (2020). Promotion effect of cerium doping on iron-titanium composite oxide catalysts for selective catalytic reduction of NO_x with NH_3. Catalysis Science & Technology, 10(3): 648–657

Zhang W, Shi X, Yan Z, Shan Y, Zhu Y, Yu Y, He H (2021a). Design of high-performance iron-niobium composite oxide catalysts for NH_3-SCR: Insights into the interaction between Fe and Nb. ACS Catalysis, 11(15): 9825–9836

Zhang Z, Li R, Wang M, Li Y, Tong Y, Yang P, Zhu Y (2021b). Two steps synthesis of $CeTiO_x$ oxides nanotube catalyst: Enhanced activity, resistance of SO_2 and H_2O for low temperature NH_3-SCR of NO_x. Applied Catalysis B: Environmental, 282: 119542–119553

Zhu M, Lai J K, Tumuluri U, Wu Z, Wachs I E (2017). Nature of active sites and surface intermediates during SCR of NO with NH_3 by supported V_2O_5-WO_3/TiO_2 catalysts. Journal of the American Chemical Society, 139(44): 15624–15627